

# We are IntechOpen, the world's leading publisher of Open Access books Built by scientists, for scientists

6,900

Open access books available

185,000

International authors and editors

200M

Downloads

Our authors are among the

154

Countries delivered to

TOP 1%

most cited scientists

12.2%

Contributors from top 500 universities



WEB OF SCIENCE™

Selection of our books indexed in the Book Citation Index  
in Web of Science™ Core Collection (BKCI)

Interested in publishing with us?  
Contact [book.department@intechopen.com](mailto:book.department@intechopen.com)

Numbers displayed above are based on latest data collected.  
For more information visit [www.intechopen.com](http://www.intechopen.com)



---

# **Steady-State and Transient Performance Analysis of Permanent-Magnet Machines Using Time-Stepping Finite Element Technique**

---

Kazumi Kurihara

Additional information is available at the end of the chapter

<http://dx.doi.org/10.5772/48426>

---

## **1. Introduction**

Recently, global warming has become an important problem. High-efficiency machines have been needed in a large variety of industrial products in order to save electrical energy. For many applications, permanent-magnet (PM) synchronous machines can be designed which is smaller in size but more efficient as compared to induction machines [1-3]. Besides, PMs have been employed as an alternative to current carrying coils for magnetic field excitation in synchronous machines for over 50 years. The lack of slip rings, brushes and field winding losses have always been viewed as distinct advantages over that of conventional wound field machines. However, when the machine size becomes small, the efficiency becomes low. This is mainly due to the reason that the iron loss and the copper loss are large, because the iron core of the stator in the small machine generally does not have annealing and the resistance of the stator windings is comparatively large.

This chapter presents a successful design of the high-efficiency small but novel Interior permanent-magnet (IPM) machines using Neodymium-Boron-Iron (NdBFe) magnets. It is designed to operate with both high-efficiency line-start IPM motors [3] and generators with damper bars [4]. Time-stepping finite element analysis has been used to successfully predict the dynamic and transient performances of the prototype machines. Time-stepping finite element analysis [3-6] has been used to successfully predict the dynamic and transient performances of the prototype IPM machines. The computed performance has been validated by tests in the prototype machine.

## 2. IPM machine configuration

The photograph of an IPM rotor, the cross section of a quarter of the high-efficiency motor and the demagnetization curve of the NdBFe magnet used for finite-element analysis are shown respectively in Figures 1-3, respectively [3].

A frame size of a 600 W, 3-phase, 4-pole, Y-connected, 50 Hz, 200 V squirrel-cage induction machine was used for testing the IPM rotor shown in Figure 1. The four-pole magnets arrangement in the rotor is oriented for a high-field type IPM synchronous machine. The experimentally developed rotor has the following distinctive design features [3]:

1. The fluxes from both sides of the magnet are concentrated effectively in the middle of the magnetic poles of the rotor.
2. The reluctance of the d axis is larger than that of the q axis, because the d- axis flux passes across the magnet with high reluctance. Large reluctance torque can be obtained.
3. The conducting material between the magnet and the rotor core is made from aluminum and has both functions of the flux barrier and cage bar.

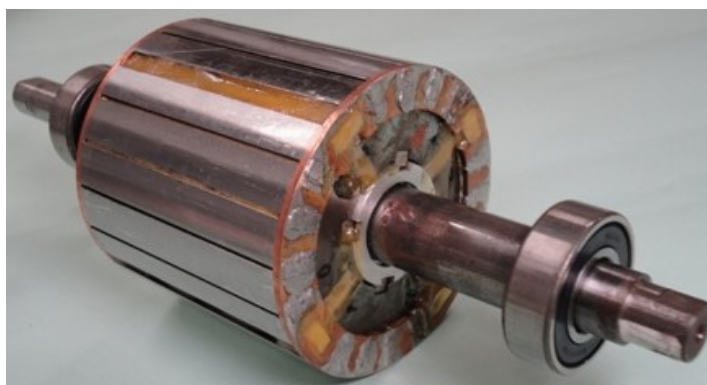


Figure 1. IPM rotor

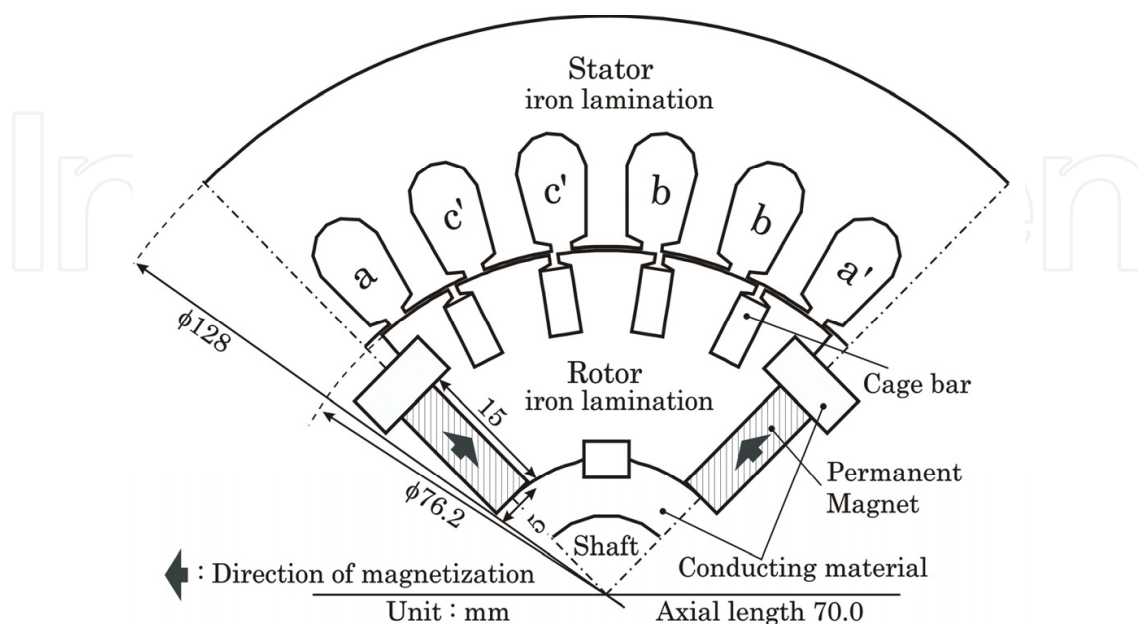
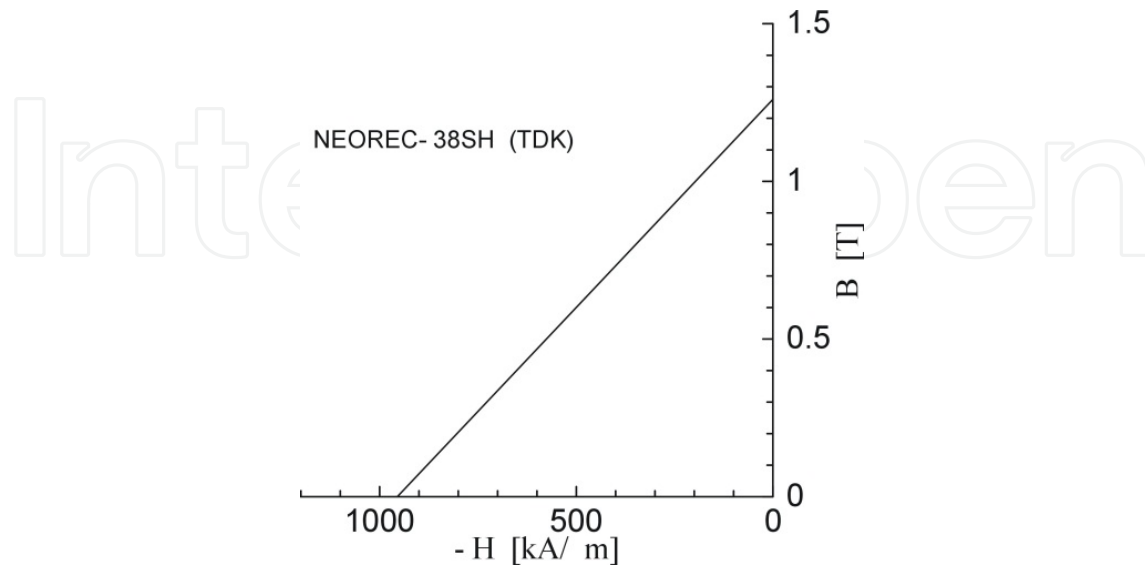


Figure 2. Configuration of high-efficiency IPM machine

Furthermore, the number and configuration of rotor slots have been successfully designed by using the finite-element method so that the waveform of the electromotive force (EMF) due to the PMs was close to the sine waveform and the cogging torque was low.



**Figure 3.** Demagnetization curve of NdBF magnet

### 3. Method for analysis

The analysis for taking the eddy currents into account, in general becomes essential to solve the three-dimensional problem. In this paper, it is assumed that the eddy currents flow approximately in the axial direction, because the rotor shown in Figure 1 is equipped with end rings. This reduces the analysis to a two-dimensional problem. The fundamental equations for the magnetic field are represented in the two-dimensional rectangular co-ordinates as

$$\frac{\partial}{\partial x} \left( \nu \frac{\partial A}{\partial x} \right) + \frac{\partial}{\partial y} \left( \nu \frac{\partial A}{\partial y} \right) = -J_0 - J_e - J_m \quad (1)$$

$$J_e = -\sigma \frac{\partial A}{\partial t} \quad (2)$$

$$J_m = \nu_0 \left( \frac{\partial M_y}{\partial x} - \frac{\partial M_x}{\partial y} \right) \quad (3)$$

where  $A$  is the  $z$  component of magnetic vector potential  $A$ ,  $J_0$  is the stator-winding current density,  $J_e$  is the eddy current density,  $J_m$  is the equivalent magnetizing current density,  $M_x$ ,  $M_y$  are  $x$  and  $y$  components of the magnetization  $\mathbf{M}$ , respectively.  $\sigma$  is the conductivity, and  $\nu$  is the reluctivity. The value of  $\nu$  in the PM is assumed the same as the reluctivity of free space  $\nu_0$ .  $J_m$  is assumed zero, outside the PM.

The effect of the eddy current for the rotor ends is taken into account by multiplying by the coefficient  $k_c$  as described below. It is done to reduce the analysis to two-dimensional. The

equivalent resistance  $R_2$  for rotor bars including the rotor end rings can be given below if the bars are distributed at equal intervals in the rotor [7].

$$R_2 = R_b + R_e \frac{Z_2}{(2p\pi)^2} \quad (4)$$

where  $R_b$  is the resistance of a bar,  $R_e$  is the resistance of the end rings,  $Z_2$  is the number of rotor slots and  $p$  is the pole pair number.

Therefore,  $k_c$  is given by

$$k_c = \frac{R_b}{R_2} \quad (5)$$

This coefficient  $k_c$  is found effective to take into account the rotor-bar current for the fundamental space harmonic. Moreover, it has been found that the agreement between computed and measured results of the starting performance characteristics in the IPM motor is good [3]. Therefore, it is considered that design use of the  $k_c$  is acceptable, even if the higher space harmonics exists [5]. The value of coefficient  $k_c$  is 0.55 in this paper.

### 3.1. Voltage, current and dynamic equations and calculation steps for IPM synchronous motor

Figure 4 shows the circuit of the three-phase line-start IPM synchronous motor. It has three stator phase windings, which are star connected with neutral. The voltage and current equations of the IPM motor are given as

$$e_a + r_1 i_a + L_1 \frac{\partial i_a}{\partial t} = v_a - v_n \quad (6)$$

$$e_b + r_1 i_b + L_1 \frac{\partial i_b}{\partial t} = v_b - v_n \quad (7)$$

$$e_c + r_1 i_c + L_1 \frac{\partial i_c}{\partial t} = v_c - v_n \quad (8)$$

$$i_a + i_b + i_c = 0 \quad (9)$$

where  $v_a$ ,  $v_b$ , and  $v_c$  are the phase voltages, subscripts  $a$ ,  $b$ , and  $c$  represent stator quantities in lines  $a$ ,  $b$ , and  $c$ , respectively.  $v_n$  is the potential of the neutral  $n$ , when the potential of the neutral of the supply source is zero,  $i_a$ ,  $i_b$ , and  $i_c$  are the line currents,  $r_1$  and  $L_1$  are the resistance and end-winding leakage inductance of the stator winding per phase, respectively.  $e_a$ ,  $e_b$ , and  $e_c$  are the induced phase voltages; and  $e_a$  is given by the line integral of the vector potential round  $c_a$  which is along the stator windings of phase  $a$  [5]

$$e_a = \oint_{c_a} \frac{\partial A^t}{\partial t} ds = \oint_{c_a} \frac{A^t - A^{t-\Delta t}}{\Delta t} ds \quad (10)$$

where  $A^t$  is  $A$  at time  $t$ .  $\Delta t$  is the time step.  $e_b$ , and  $e_c$  can be obtained similarly, as in [5].

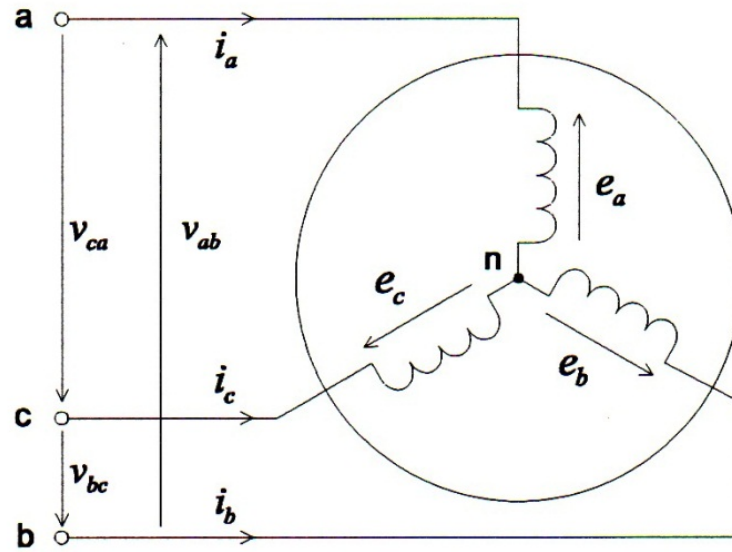


**Figure 4.** Circuit of three-phase line-start IPM synchronous motor

For operation from a balanced three-phase system,

$$v_a + v_b + v_c = 0. \quad (11)$$

$v_n$  can be obtained by adding each side of (6)-(8) and then applying (9) and (11)

$$v_n = \frac{e_a + e_b + e_c}{3}. \quad (12)$$

One obtains the following equation by substituting (12) in (6)-(8) [5]:

$$\frac{2}{3}e_a - \frac{e_b + e_c}{3} + r_1 i_a + L_1 \frac{\partial i_a}{\partial t} - v_a = 0 \quad (13)$$

$$\frac{2}{3}e_b - \frac{e_c + e_a}{3} + r_1 i_b + L_1 \frac{\partial i_b}{\partial t} - v_b = 0 \quad (14)$$

$$\frac{2}{3}e_c - \frac{e_a + e_b}{3} + r_1 i_c + L_1 \frac{\partial i_c}{\partial t} - v_c = 0. \quad (15)$$

The dynamic equation is given as [3]

$$T = J \frac{d\omega_r}{dt} + B_0 \omega_r + T_l \quad (16)$$

where  $T$  is the instantaneous electromagnetic torque,  $J$  is the rotational inertia,  $\omega$  is the rotor angular speed,  $B_0$  is the friction coefficient, and  $T_l$  is the load torque. The torque  $T$  is calculated by using the *Bil* rule [8]. The angular speed,  $\omega$  is given by

$$\omega_r = \frac{d\theta}{dt} \quad (17)$$

where  $\theta$  is the rotational angle of the rotor.

One obtains the following equation by substituting (17) in (16):

$$T = J \frac{d^2\theta}{dt^2} + B_0 \frac{d\theta}{dt} + T_l. \quad (18)$$

In this paper, the forward difference method is used to obtain the rotational angle at time  $t$  because the vector potential, currents and rotational angle at time  $t - \Delta t$  are all known

$$\frac{d\theta^{t-\Delta t}}{dt} = \frac{\theta^t - \theta^{t-\Delta t}}{\Delta t} \quad (19)$$

$$\frac{d^2\theta^{t-\Delta t}}{dt^2} = \frac{\theta^t - 2\theta^{t-\Delta t} + \theta^{t-2\Delta t}}{(\Delta t)^2}. \quad (20)$$

One obtains the following equation by substituting (19) and (20) in (18) [6]:

$$\theta^t = \frac{1}{J + B_0\Delta t} [(T^{t-\Delta t} - T_l^{t-\Delta t})(\Delta t)^2 + (2J + B_0\Delta t)\theta^{t-\Delta t} - J\theta^{t-2\Delta t}]. \quad (21)$$

In the case when the effect of the friction is negligibly small, the above equation can be represented simply as follows:

$$\theta^t = \frac{(\Delta t)^2}{J} (T^{t-\Delta t} - T_l^{t-\Delta t}) + 2\theta^{t-\Delta t} - \theta^{t-2\Delta t}. \quad (22)$$

One can obtain the vector potential, currents and rotational angle by solving (1), (13)-(15), and (18) using the time-stepping finite element technique [3].

Next, the calculation steps for this analysis are shown in Figure 5.

1. First, the terminal voltage  $V_l$ , its initial phase angle  $\phi$ ,  $T_l$ , and  $\Delta t$  are set, respectively. Each voltage for the three stator phase windings can be represented by

$$v_a^t = \sqrt{\frac{2}{3}} V_l \cos(\omega t + \phi_0) \quad (23)$$

$$v_b^t = \sqrt{\frac{2}{3}} V_l \cos\left(\omega t + \phi_0 - \frac{2}{3}\pi\right) \quad (24)$$

$$v_c^t = \sqrt{\frac{2}{3}} V_l \cos\left(\omega t + \phi_0 - \frac{4}{3}\pi\right). \quad (25)$$

2. The vector potential  $A$  at  $t = 0$  is set, where the static field caused by only PMs is given as the initial value.
3. At  $t = \Delta t + t$ , the value of  $\theta^t$  at new  $t$  is set.
4. At  $t = \Delta t + t$ , each voltage at new  $t$  is set.
5. The initial values for  $A^t$ ,  $i_a^t$ ,  $i_b^t$ , and  $i_c^t$  are set.
6. The matrix equation constructed by the time-stepping finite element technique is solved [5].
7. The convergence of  $A^t$  is tested. Unless  $A^t$  converges, the process returns to step 6).
8. After the convergence of  $A^t$ ,  $i_a^t$ ,  $i_b^t$ , and  $i_c^t$ ,  $T^t$  can be calculated. Then, the  $\theta^t$  is determined from (22).
9. The calculation process from step 3) to step 7) continues till the steady-state currents are obtained.

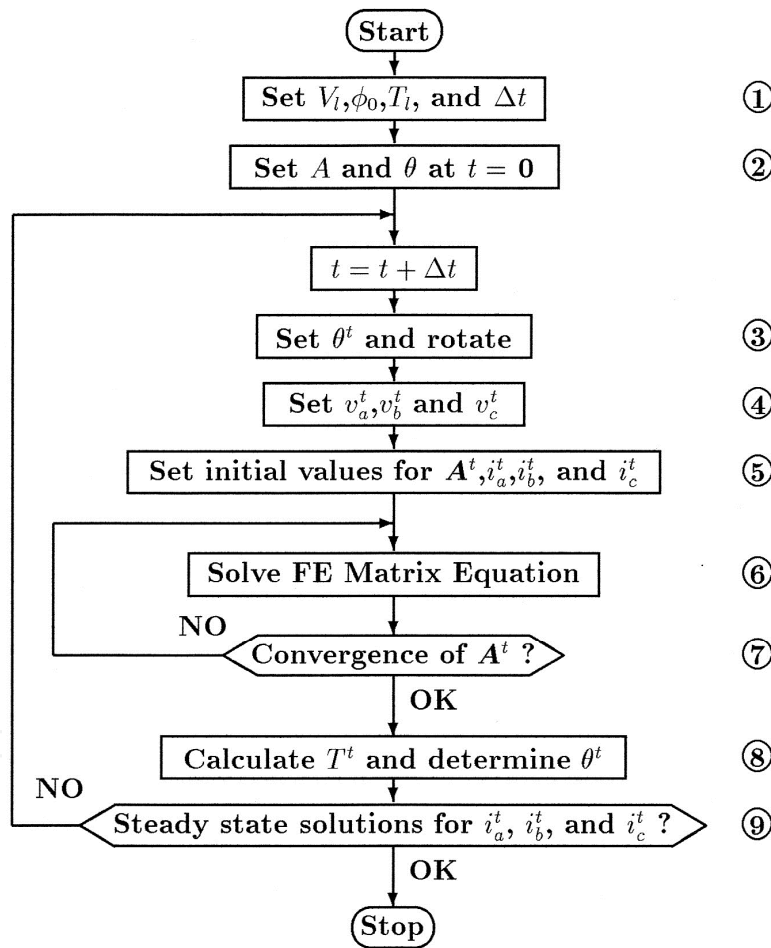


**Figure 5.** Flowchart of three-phase line-start IPM synchronous motor

### 3.2. Voltage and current equations and calculation steps for IPM synchronous generator

Figure 6 shows the circuit of the three-phase IPM synchronous generator. The voltage and current equations of the IPM generator are given as



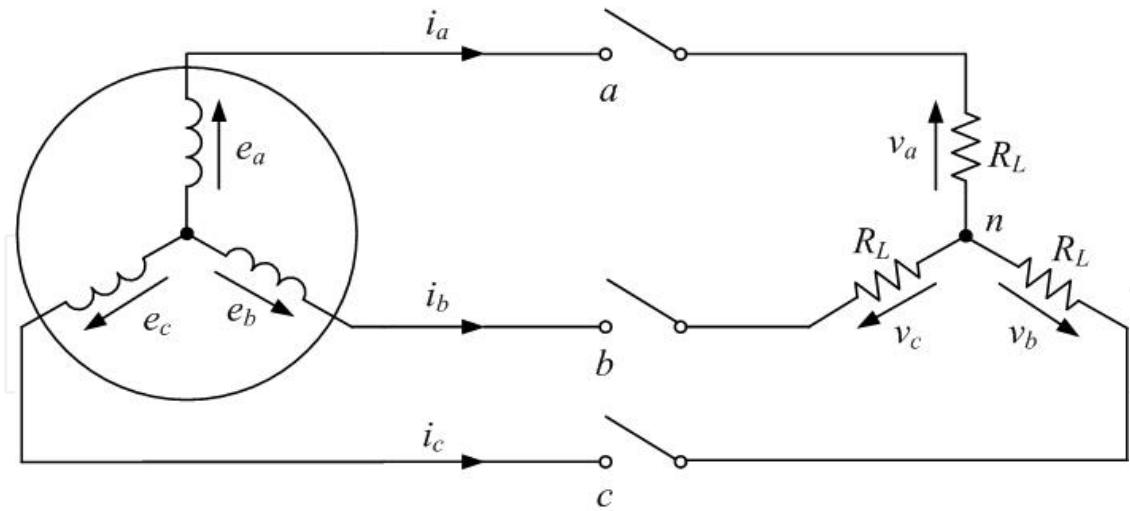


**Figure 6.** Circuit of three-phase IPM synchronous generator

$$e_a = r_1 i_a + L_1 \frac{\partial i_a}{\partial t} + v_a + v_n \quad (26)$$

$$e_b = r_1 i_b + L_1 \frac{\partial i_b}{\partial t} + v_b + v_n \quad (27)$$

$$e_c = r_1 i_c + L_1 \frac{\partial i_c}{\partial t} + v_c + v_n \quad (28)$$

For a balanced three-phase resistance load,

$$v_a = R_L i_a, \quad v_b = R_L i_b, \quad v_c = R_L i_c \quad (29)$$

where  $R_L$  is a load resistance per phase.

$v_n$  can be obtained by substituting (29) in (26)-(28), adding each side of (26)-(28) and then applying (9)

$$v_n = \frac{e_a + e_b + e_c}{3} \quad (30)$$

One obtains the following equation by substituting (30) in (26)-(28).

$$\frac{2}{3} e_a - \frac{e_b + e_c}{3} - (r_1 + R_L) i_a - L_1 \frac{\partial i_a}{\partial t} = 0 \quad (31)$$

$$\frac{2}{3} e_b - \frac{e_c + e_a}{3} - (r_1 + R_L) i_b - L_1 \frac{\partial i_b}{\partial t} = 0 \quad (32)$$

$$\frac{2}{3} e_c - \frac{e_a + e_b}{3} - (r_1 + R_L) i_c - L_1 \frac{\partial i_c}{\partial t} = 0 \quad (33)$$

One can obtain the vector potential, currents by assuming a constant speed and then solving (1), (31)-(33) using the time-stepping finite-element technique [5].

Next, the calculation steps for this analysis are shown in Figure 7.

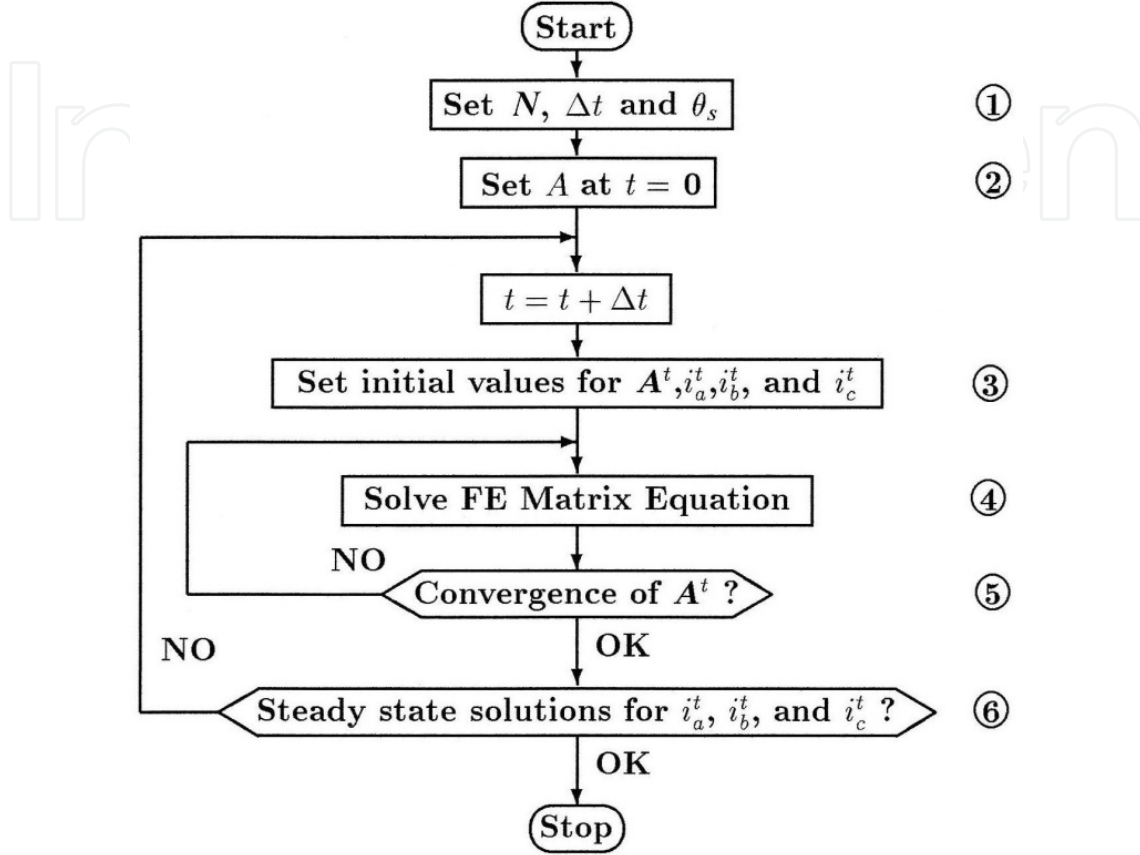


**Figure 7.** Flowchart of three-phase IPM synchronous generator

1. First,  $N$ ,  $\Delta t$  and the corresponding rotational step  $\theta_s$  are set, respectively.
2. The vector potential  $A$  at time  $t = 0$  is set, where the static field caused by only PMs is given as the initial value.
3. At  $t = t + \Delta t$ , the initial values for  $A^t$ ,  $i_a^t$ ,  $i_b^t$  and  $i_c^t$  at new  $t$  are set.
4. The matrix equation constructed by the time-stepping finite-element technique is solved [5].
5. The convergence of  $A^t$  is tested. Unless  $A^t$  converges, the process returns to step 4).
6. After the convergence of  $A^t$ ,  $i_a^t$ ,  $i_b^t$  and  $i_c^t$  are obtained. The calculation process from step 3) to 5) continues till the steady-state currents are obtained.

#### 4. Steady-state synchronous and transient performance

This paper contains the steady-state synchronous and transient performance characteristics of the IPM synchronous machine shown in Figure 2. The good agreement between computed and measured results validates the proposed method for the finite-element analysis to predict the machine performance exactly.

4.1. EMF due to PMs

Figure 8 shows the terminal voltage waveform generated by PMs in driving the IPM synchronous machine at 1500 r/min by the external motor. It is shown that the agreement between the computed and measured values of the generated voltage is excellent.

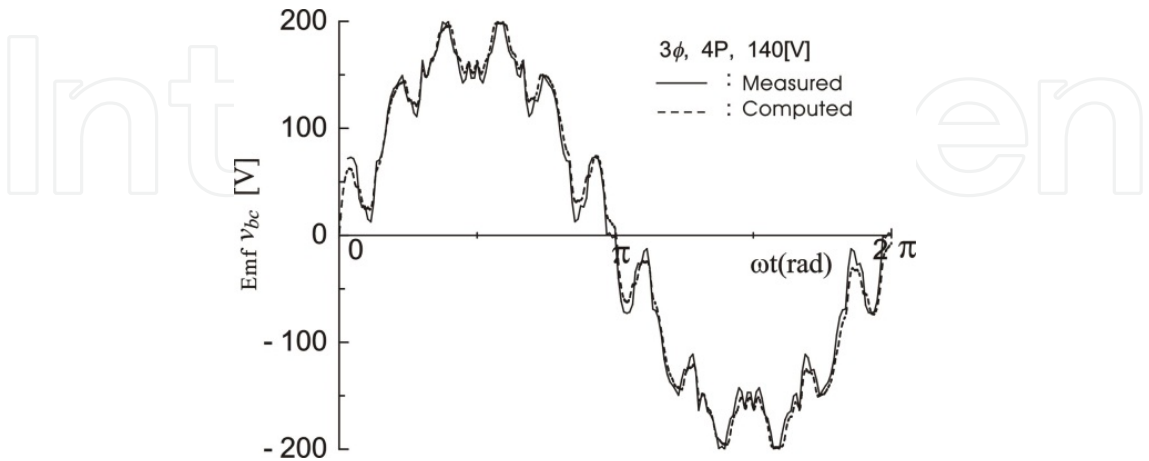


Figure 8. EMF generated by PMs

4.2. Steady-state synchronous and transient performance of Line-start IPM synchronous motor

Figure 9 shows the load performance characteristics at 140V. It is clear from Figure 9 that the power factor is almost unity at all loads. The efficiency and power factor of the IPM motor were 86.2% and 0.986, respectively for the output of 600 W. The efficiency-power-factor product is 85.0%. It is about 35% higher than that for the induction motor. These values of the IPM motor are very high when compared to those of the induction motor for the same 600 W nameplate rating [3]. Figure 10 shows the computed and measured results of the input current versus the output power at 140V. It is shown that the agreement between the measured and computed results is excellent.

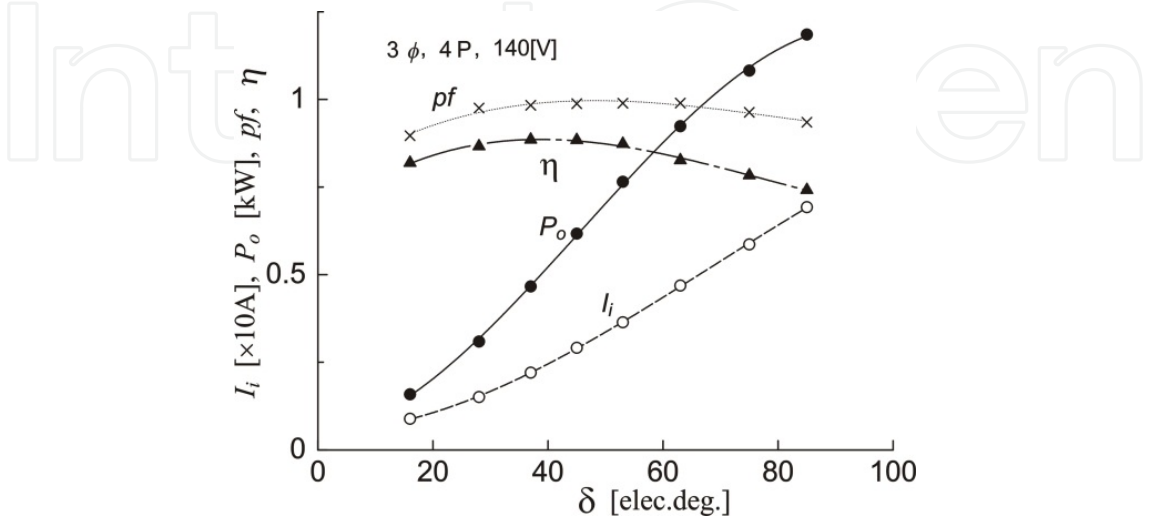
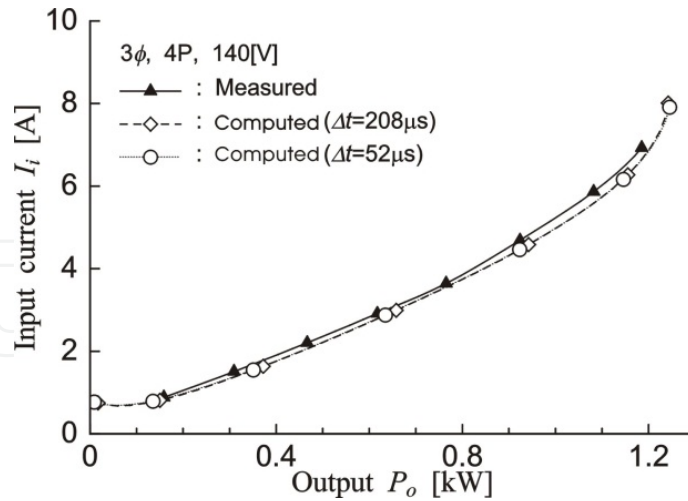


Figure 9. Measured results of load performance characteristics of IPM motor



**Figure 10.** Computed and measured results of current versus output power of IPM motor

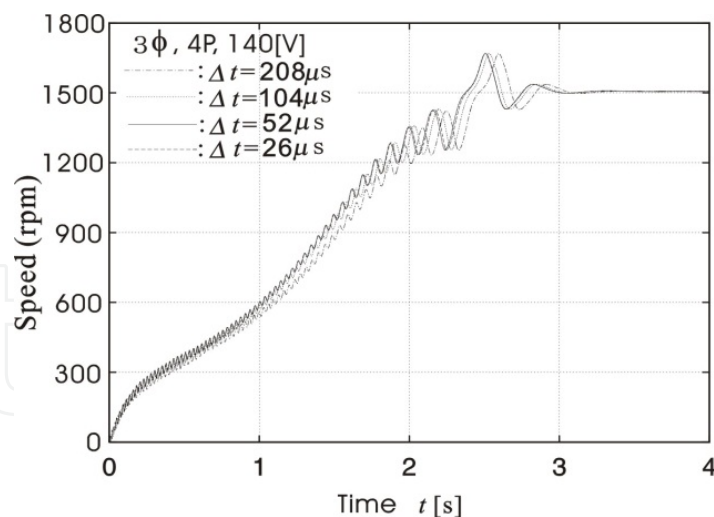
In the figure 10, two kinds of computed curves are given, and the agreement is also good. It is used to determine the suitable value of the  $\Delta t$ . This value must be determined by taking into account the effects due to the space harmonics [5]. The space harmonics effect is also the source of the cogging and ripple torques in the IPM motor. It can be compensated by skewing the stator by one slot pitch. Therefore,  $\Delta t$  should be smaller than  $\Delta t_s$  to include the influence of the ripple harmonics on the starting with  $\Delta t_s$ , which is to move by one stator slot pitch at synchronous speed of the motor

$$\Delta t_s = \frac{(1/f)}{(N_s/p)} \quad (34)$$

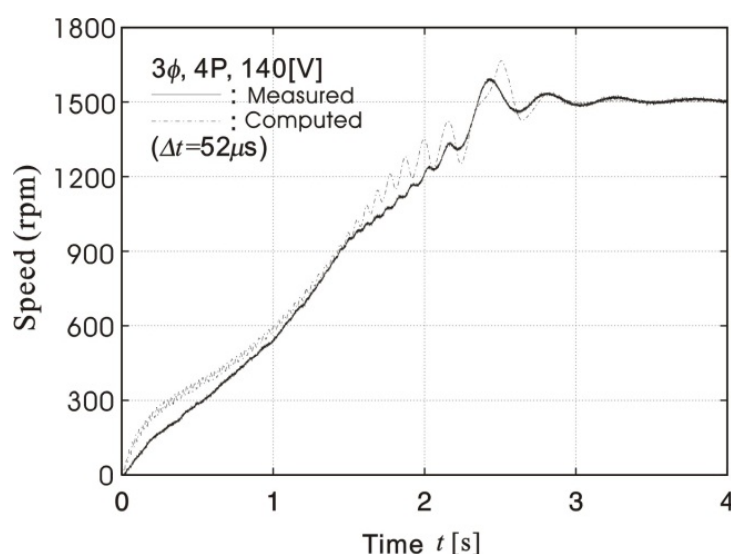
where  $f$  is the line frequency,  $N_s$  is the number of stator slots. Herein, the following four values for the  $\Delta t$  are chosen: 208, 104, 52 and 26  $\mu s$  are an eighth, a sixteenth, a thirty-second, and a sixty-fourth of  $\Delta t_s$ , respectively. It is evident from Figure 10 that the choice of 208  $\mu s$  is suitable at synchronous speed. However, this value is not sufficient in starting the IPM motor with large load inertia.

Figure 11 shows the computed speed-time responses at no load condition with the eddy-current brake disc coupled to the shaft, when the stator of the motor was supplied with balanced three-phase voltages at rated frequency of 50 Hz and rated voltage 140 V. The inertia of the disc is about 18 times the experimental rotor inertia, and the initial phase angle  $\phi$  of (23-25) is  $\pi/2$  in the figure. It is seen that the agreement between the curves of 52  $\mu s$  and 26  $\mu s$  is good and that those are superposed. The choice of a time step of 52  $\mu s$  is suitable when the starting of the IPM motor.

Figure 12 shows the computed and measured speed-time responses with time during run-up and synchronizing period when  $\Delta t$  and  $\phi$  are 52  $\mu s$  and  $\pi/2$ , respectively. It can be seen that the good agreement between the measured and computed results exists.



**Figure 11.** Computed speed-time response of IPM motor



**Figure 12.** Computed and measured speed-time response of IPM motor

#### 4.3. Steady-state synchronous and transient performance of IPM synchronous generator

Figure 13 shows the experimental setup for measuring the steady-state load performance characteristics of the IPM generator shown in Figure 2. A 2.2 kW three-phase two-pole 50 Hz 200 V squirrel-cage induction motor and a torque detector were used. The IPM generator has been driven at 1500 r/min by the PWM inverter-driven induction motor.

Figures 14-17 show the terminal voltage and line current, respectively, when the IPM generator with the cage-bars was changed from no-load to resistance load of  $15 \Omega$  per phase in Figure 6 at  $t = 0$ s. The values of the resistance per phase for the maximum load was  $15 \Omega$ . A synchronous motor has been used as the prime mover in the experiment.

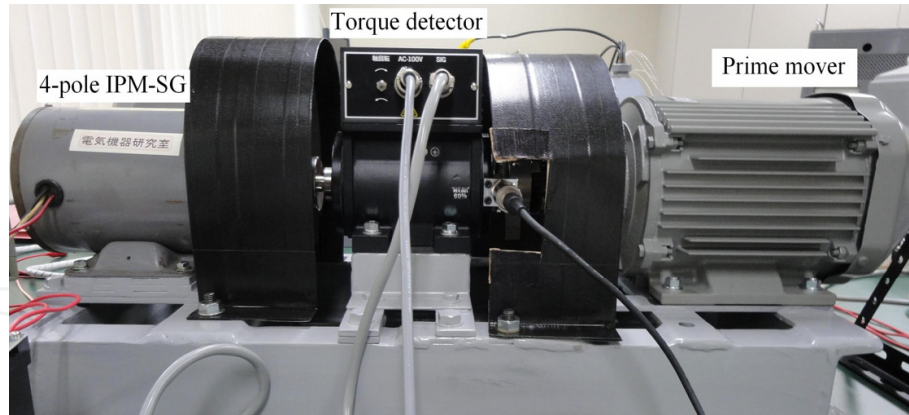


**Figure 13.** Experimental setup for IPM synchronous generator

Figures 14 and 15 show the measured and computed results of the terminal voltage, respectively. The phase angle of the terminal voltage in computing the terminal voltage and current is fitted to the experimental one. It is seen that the good agreement exists between the measured and computed results of the terminal voltage except the difference of the phase. This is the reason why the rotor speed lags synchronous speed in the experiment when load changes rapidly.

Figures 16 and 17 show the measured and computed results of the line current, respectively. The line current is zero before  $t = 0$ s because of no-load. It is seen that the amplitude of the measured current was slightly pulsating because of the mechanical dynamic transient. On the other hand, a constant speed has been assumed in simulation. It is, however, seen that the good agreement exists between the measured and computed results of the current except the difference of the phase.

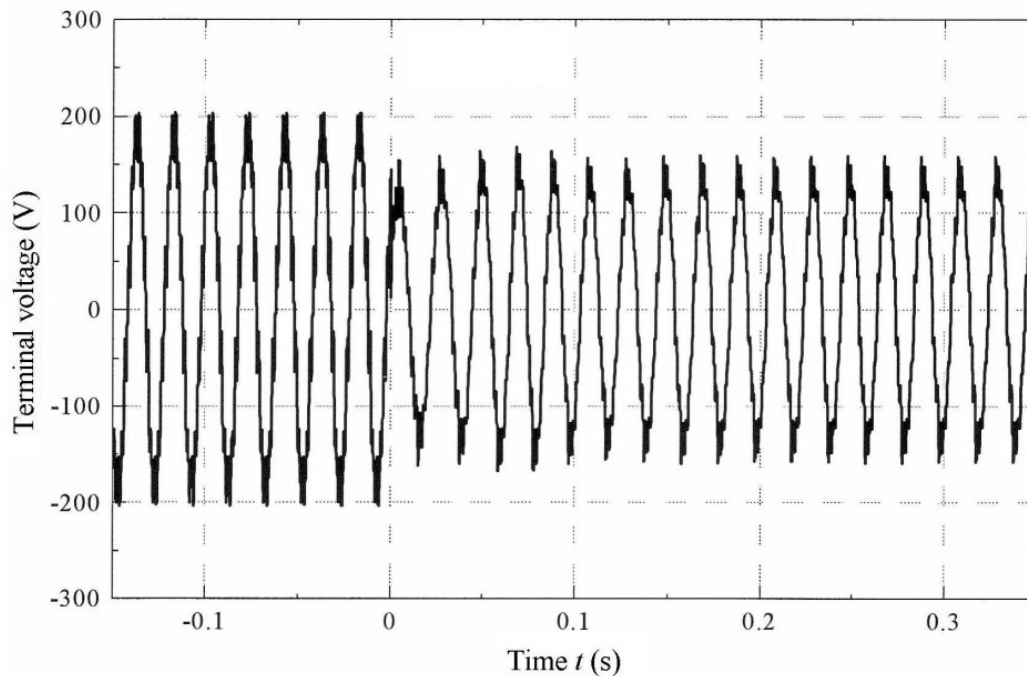


**Figure 14.** Measured results of terminal voltage versus time in IPM generator



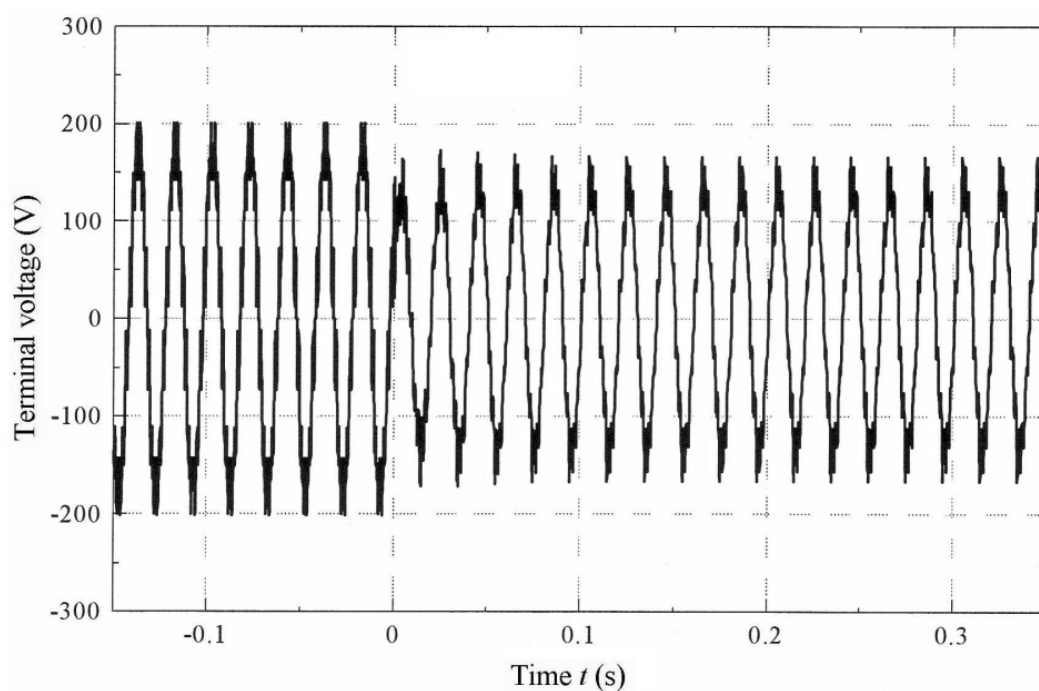


**Figure 15.** Computed results of terminal voltage versus time in IPM generator

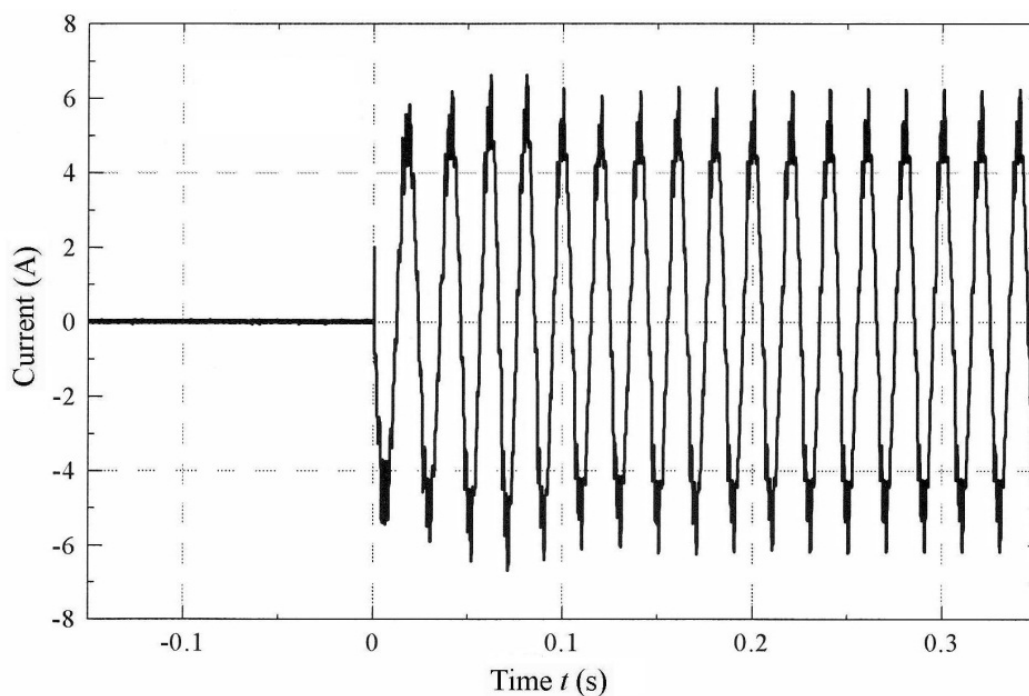


**Figure 16.** Measured results of line current versus time in IPM generator

Figures 18 and 19 show the measured and computed results of the steady-state terminal voltage and line current respectively. It is seen that the good agreement exists between the measured and computed results of the terminal voltage and line current. It is shown that the higher harmonic components by the higher space harmonics [5] were included.

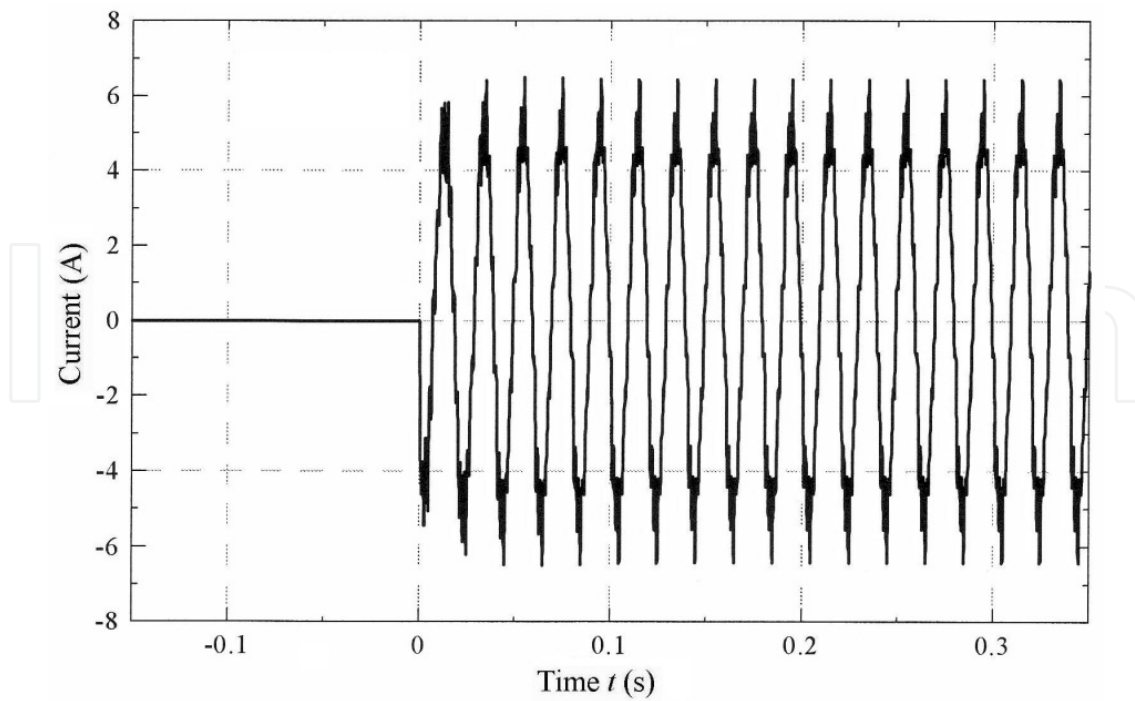


**Figure 17.** Computed results of line current versus time in IPM generator

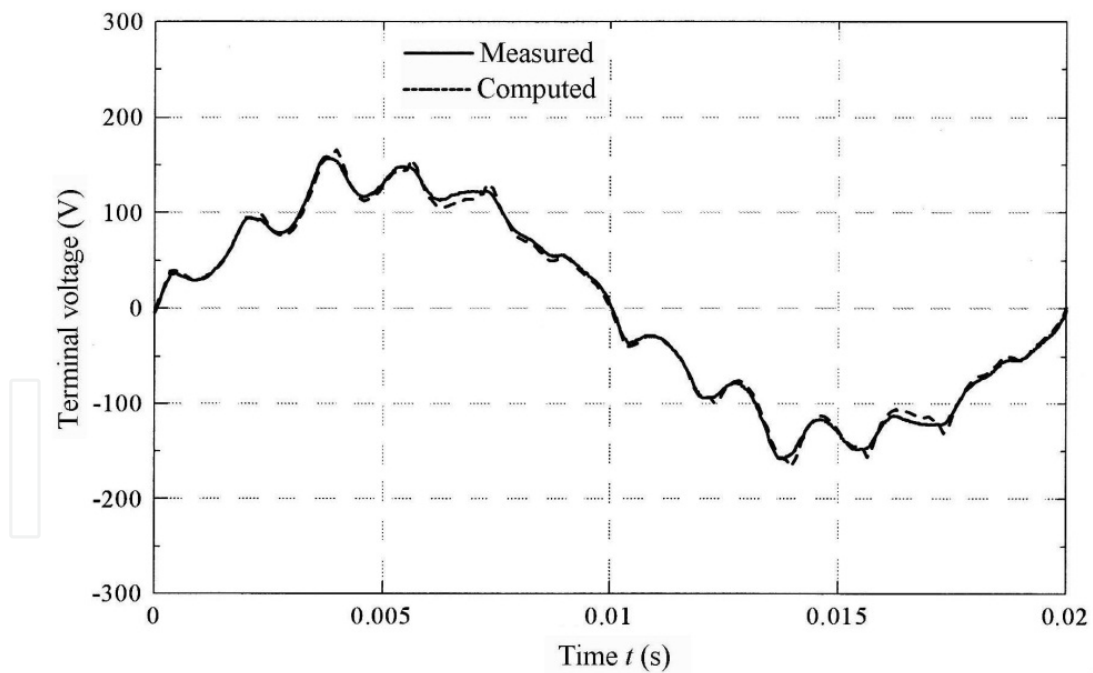
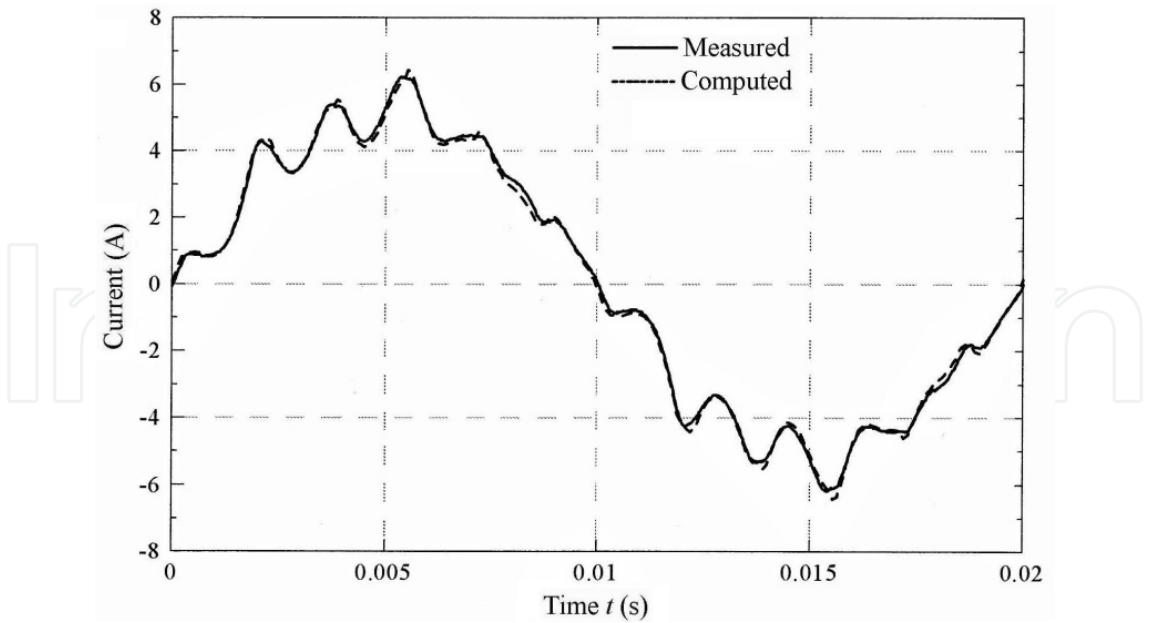


**Figure 18.** Steady-state terminal voltage versus time in IPM generator

Figures 20-22 show the steady-state load characteristics.

Figure 20 shows the measured and computed results of the terminal voltage versus the output. It can be seen that the good agreement between the measured and computed values exists except near maximum output.

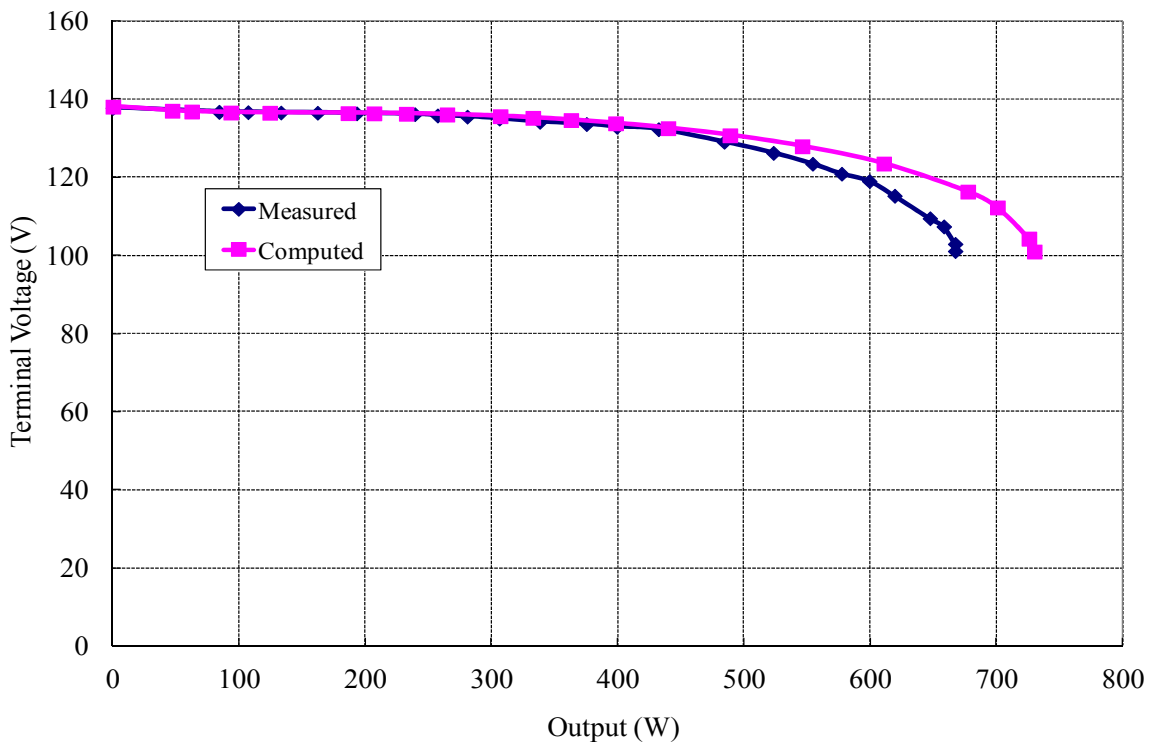




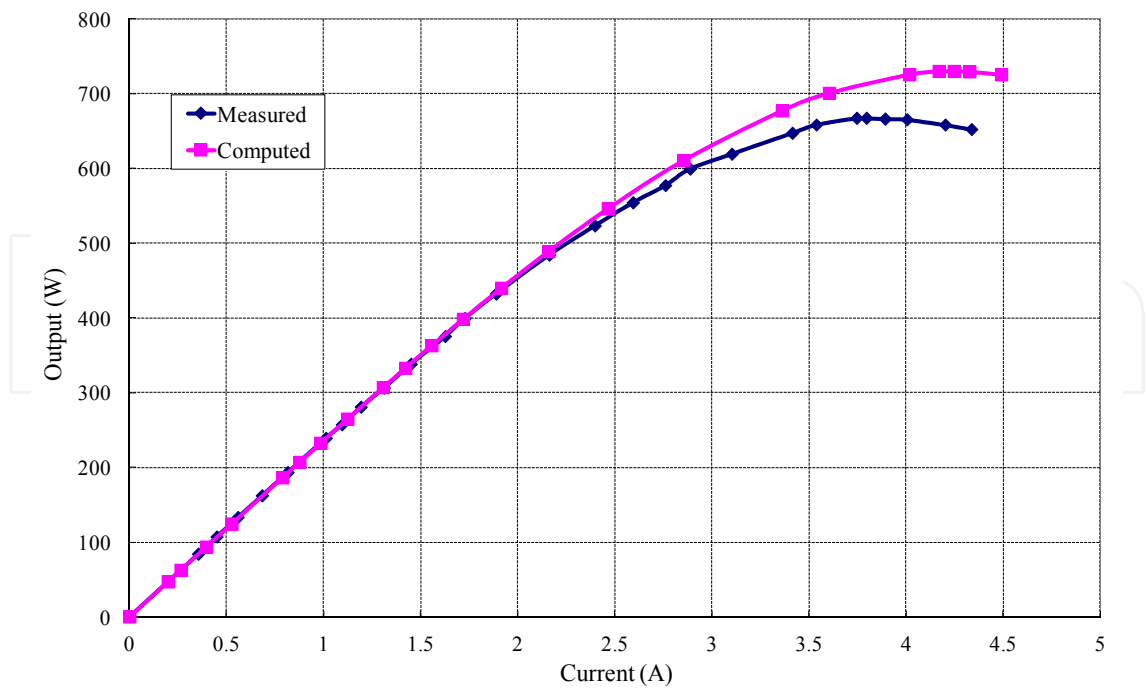
**Figure 19.** Steady-state line current versus time in IPM generator

Figure 21 shows the measured and computed results of the line current versus the output. It can be seen that the good agreement between the measured and computed values exists except near maximum output.

Figure 22 shows the measured results of the efficiency versus output. The efficiency was 85.8% at 600 W and 90% at 100W of light load. It is found that the efficiency is very high.



**Figure 20.** Measured and computed results of terminal voltage versus output in IPM generator



**Figure 21.** Measured and computed results of line current versus output in IPM generator

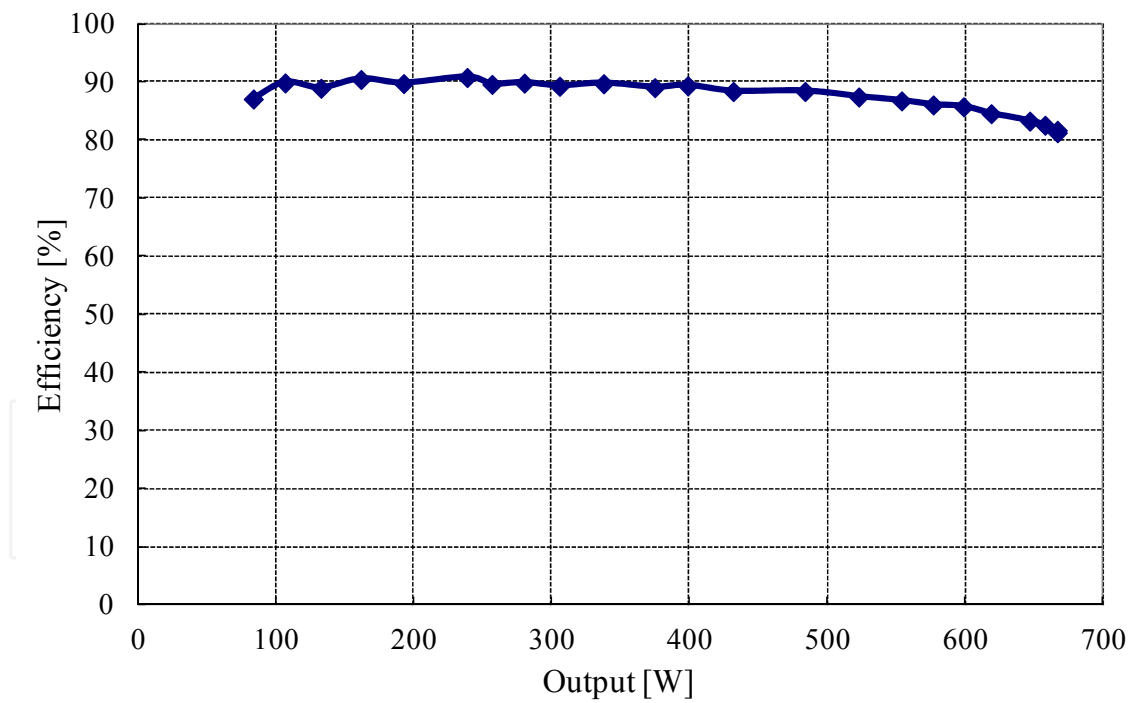


**Figure 22.** Measured results of efficiency versus output in IPM generator

## 5. Conclusion

A successful design of a high-efficiency small but novel IPM machine with cage bars was developed and tested. It is designed to operate with both high-efficiency line-start IPM

motor and generator with damper bars. The IPM motor can start and synchronize fully with large load inertia. Beside, the effects of the damper bars on stability during load change and efficiency were investigated. Time-stepping finite element analysis has been used to successfully predict the steady-state and transient performances of the prototype IPM machines. It is clear that cage bars are used effectively to start up in a line-start IPM motor, and to operate stably in the IPM generator with damper bars. It has been found that the proposed design has yielded successful simulation and experimental results.

### Author details

Kazumi Kurihara

*Department of Electrical and Electronic Engineering, Ibaraki University, Hitachi, Japan*

### Acknowledgement

The author wish to thank Dr. Marushima of the Oriental Motor Company Ltd, for technical support and T. Kubota, T. Yasui, and T. Igari of the Ibaraki University for experimental support.

### 6. References

- [1] Binns K. J, Jabbar M.A (1981) High-field self-start permanent magnet synchronous motor. Proc. IEE. B. 128:157-160.
- [2] Rahman M. A, Osheiba A. M (1990) Performance of a large line-start permanent magnet synchronous motor. IEEE Trans. Energy Conversion 5: 211-217.
- [3] Kurihara K, Rahman M. A (2004) High-efficiency line-start interior permanent-magnet synchronous motors. IEEE Trans. Ind. Applicat. 40: 789-796.
- [4] Kurihara K (2010) Effects of Cage-Bars for Stability of Interior Permanent-Magnet Synchronous Generators. Int. Conf .Elect. Mach. and Systems.
- [5] Kurihara K, Wakui G, Kubota T (1994) Steady-state performance analysis of permanent magnet synchronous motors including space harmonics. IEEE Trans. Magn. 30: 1306-1315.
- [6] Kurihara K, Monzen T, Hori M (2006) Steady-state and transient performance analysis for line-start permanent-magnet synchronous motors with skewed slots. Int. Conf.Elect. Mach.
- [7] Takeuchi J (1993) Design of Electrical Machines, Tokyo Ohmsha.
- [8] Binns K.J, Riley C.P, Wong M (1985) The efficient evaluation of torque and field gradient in permanent-magnet machines with small air-gap. IEEE Trans. Magn. 21: 2435-2438.